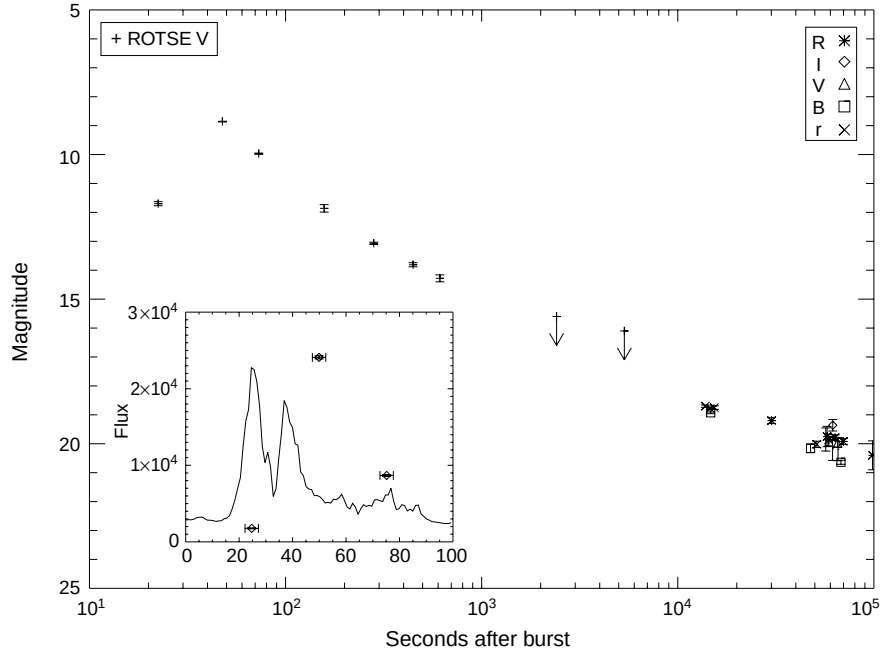

Figure 2 A combined optical light curve. Afterglow data points are drawn from the GCN archive[21–33]. The early decay of the ROTSE-I light curve is not well fitted by a single power law. The final ROTSE limit is obtained by co-adding the final four 200-s images. The inset shows the first three ROTSE optical fluxes compared to the BATSE γ-ray light curve in the 100–300 keV energy band. The ROTSE-1 fluxes are in arbitrary units. Horizontal error bars indicate periods of active observation. We note that there is no information about the optical light curve outside these intervals. Vertical error bars represent flux uncertainties. Further information about GCN is available at http://gcn.gsfc.nasa.gov/gcn

for such events. We expect that ROTSE will be important in the exploration to come. □

Received 5 February; accepted 19 February 1999.

1. Klebesadel, R. W., Strong, I. B. & Olson, R. A. Observations of gamma-ray bursts of cosmic origin. *Astrophys. J.* **182,** L85–L88 (1973).
2. Piro, L. *et al.* The first X-ray localization of a γ-ray burst by BeppoSAX and its fast spectral evolution. *Astron. Astrophys.* **329,** 906–910 (1998).
3. Costa, E. *et al.* Discovery of an X-ray afterglow associated with the γ-ray burst of 28 February 1997. *Nature* **387,** 783–785 (1997).
4. Krimm, H. A., Vanderspek, R. K. & Ricker, G. R. Searches for optical counterparts of BATSE gamma-ray bursts with the Explosive Transient Camera. *Astron. Astrophys. Suppl.* **120,** 251–254 (1996).
5. Hudec, R. & Soldán, J. Ground-based optical CCD experiments for GRB and optical transient detection. *Astrophys. Space Sci.* **231,** 311–314 (1995).
6. Lee, B. *et al.* Results from Gamma-Ray Optical Counterpart Search Experiment: a real time search for gamma-ray burst optical counterparts. *Astrophys. J.* **482,** L125–L129 (1997).
7. Park, H. S. *et al.* New constraints on simultaneous optical emission from gamma-ray bursts measured by the Livermore Optical Transient Imaging System experiment. *Astrophys. J.* **490,** L21–L24 (1997).
8. Kelson, D. D., Illingworth, G. D., Franx, M., Magee, D. & van Dokkum, P. G. *IAU Circ.* No. 7096 (1999).
9. Hjorth, J. *et al. GCN Circ.* No. 219 (1999).
10. Fenimore, E. E., Ramirez-Ruiz, E., Wu, B. GRB990123: Evidence that the γ-rays come from a central engine. Preprint astro-ph9902007 at ⟨http://xxx.lanl.gov⟩ (1999).
11. Barthelmy, S. *et al.* in *Gamma-Ray Bursts: 4th Huntsville Symp.* (eds Meegan, C. A, Koskut, T. M. & Preece, R. D.) 99–103 (AIP Conf. Proc. 428, Am. Inst. Phys., College Park, 1997).
12. Piro, L. *et al. GCN Circ.* No. 199 (1999).
13. Odewahn, S. C. *et al. GCN Circ.* No. 201 (1999).
14. Bloom, J. S. *et al. GCN Circ.* No. 208 (1999).
15. Katz, J. I. Low-frequency spectra of gamma-ray bursts. *Astrophys. J.* **432,** L107–L109 (1994).
16. Mészáros, P. & Rees, M. J. Optical and long-wavelength afterglow from gamma-ray bursts. *Astrophys. J.* **476,** 232–237 (1997).
17. Sari, R. & Piran, T. The early afterglow. Preprint astro-ph/9901105 at ⟨http://xxx.lanl.gov⟩ (1999).
18. Bertin, E. & Arnouts, S. SExtractor: Software for source extraction. *Astron. Astrophys. Suppl.* **117,** 393–404 (1996).
19. Høg, E. *et al.* The Tycho reference catalogue. *Astron. Astrophys.* **335,** L65–L68 (1998).
20. Monet, D. *et al. A Catalog of Astrometric Standards* (US Naval Observatory, Washington DC, 1998).
21. Zhu, J. & Zhang, H. T. *GCN Circ.* No. 204 (1999).
22. Bloom, J. S. *et al. GCN Circ.* No. 206 (1999).
23. Gal, R. R. *et al. GCN Circ.* No. 207 (1999).
24. Sokolov, V. *et al. GCN Circ.* No. 209 (1999).
25. Ofek, E. & Leibowitz, E. M. *GCN Circ.* No. 210 (1999).
26. Garnavich, P., Jha, S., Stanek, K. & Garcia, M. *GCN Circ.* No. 215 (1999).
27. Zhu, J. *et al. GCN Circ.* No. 217 (1999).
28. Bloom, J. S. *et al. GCN Circ.* No. 218 (1999).
29. Maury, A., Boer, M. & Chaty, S. *GCN Circ.* No. 220 (1999).
30. Zhu, J. *et al. GCN Circ.* No. 226 (1999).
31. Sagar, R., Pandey, A. K., Yadav, R. K. R., Nilakshi & Mohan, V. *GCN Circ.* No. 227 (1999).
32. Masetti, N. *et al. GCN Circ.* No. 233 (1999).
33. Bloom, J. S. *et al. GCN Circ.* No. 240 (1999).

Acknowledgements. the ROTSE Collaboration thanks J. Fishman and the BATSE team for providing the data that enable the GCN localizations which made this experiment possible; and we thank the BeppoSAX team for rapid distribution of coordinates. This work was supported by NASA and the US DOE. The Los Alamos National Laboratory is operated by the University of California for the US Department of Energy (DOE). The work was performed in part under the auspices of the US DOE by Lawrence Livermore National Laboratory. BeppoSAX is a programme of the Italian Space Agency (ASI) with participation of the Dutch Space Agency (NIVR).

Correspondence and requests for materials should be addressed to C.A. (e-mail: akerlof@mich.physics.lsa.umich.edu).

A simple explanation of light emission in sonoluminescence

Sascha Hilgenfeldt*, Siegfried Grossmann† & Detlef Lohse‡

** Division of Engineering and Applied Sciences, Harvard University, 29 Oxford Street, Cambridge, Massachusetts 02138, USA*
† Fachbereich Physik der Universität Marburg, Renthof 6, D-35032 Marburg, Germany
‡ Department of Applied Physics and J. M. Burgers Centre for Fluid Dynamics, University of Twente, PO Box 217, NL-7500 AE Enschede, The Netherlands

Ultrasonically driven gas bubbles in liquids can emit intense bursts of light when they collapse[1]. The physical mechanism for single-bubble sonoluminescence has been much debated[2,3]. The conditions required for, and generated by, bubble collapse can be deduced within the framework of a hydrodynamic (Rayleigh–Plesset[4]) analysis of bubble dynamics and stability[5,6], and by considering the dissociation and outward diffusion of gases under the extreme conditions induced by collapse[7,8]. We show here that by extending this hydrodynamic/chemical picture in a simple way, the light emission can be explained too. The additional elements that we add are a model for the volume dependence of the bubble's temperature[9,10] and allowance for the small emissivity of a weakly ionized gas[11]. Despite its simplicity, our approach can account quantitatively for the observed parameter dependences of

the light intensity and pulse width, as well as for the spectral shape and wavelength independence of the pulses[12–15].

The first reliable measurements of the pulse width of single-bubble sonoluminescence (SBSL) and its virtual independence on wavelength[12–15] showed that simple Planck emission from a black body is not sufficient to explain the experimental observations, because it would result in much longer pulses at long wavelengths than in the short wavelength regime. Moss and collaborators[11] realized that the temperature-dependent photon absorption of the gas has to be taken into account to explain the deviation from black-body radiation. They found that the bubble is not an ideal absorber (that is, not a surface emitter like an ideal black body), but because of its tiny size most photons can escape without reabsorption and therefore the bubble is transparent for its own radiation most of the time (that is, it is a volume emitter). The photons carry information about the light production processes, and the radiation differs from black-body emission in both intensity and spectral shape.

To calculate the absorption coefficients (and thus the light emission) quantitatively, we need the temporal variation of the bubble radius $R(t)$ and of the gas temperature $T(t)$ inside the bubble. The bubble dynamics are well described by the Rayleigh-Plesset equation[4] and the bubble temperature, which is assumed to be spatially uniform, follows directly from $R(t)$ via the near-adiabatic compression and heating of the collapsing bubble. (The assumption of uniform bubble temperature is supported by full numerical simulations of the bubble's interior[11,16,17].) To describe the heating, we use a polytropic exponent which itself varies with time, taken from Prosperetti's work[9,10]. This leads to isothermal behaviour for most of the cycle, whereas adiabaticity is approached only near the radius minimum (see Section 1 of Supplementary Information). For the parameters of typical SBSL experiments, the maximum computed temperatures lie in a fairly narrow range of $T_{max} \approx 20{,}000$–$30{,}000$ K. (This is much higher than the 5,000 K observed in multi-bubble sonoluminescence[18].) All parameters entering the entire formalism described here are the appropriate material parameters for noble gases in water; no adjustable fitting parameters have been used. We consider only noble gases (especially argon and xenon), because all other (molecular) constituents of the gas dissociate and leave the bubble[7,8], as has been confirmed in experiment[19,20].

The computed maximum temperatures translate, via the Saha equation[21], into a rather small degree of ionization α. With ionization energies $E_{ion} \approx 16$ eV for argon and ≈ 12 eV for xenon, $\alpha \propto \exp(-E_{ion}/2k_BT)$ typically stays below a few per cent in Ar and below 10% in Xe. In this regime, three processes give the most important contributions to the photon absorption coefficient[11,21]: free–free transitions of (1) electrons near ions (bremsstrahlung absorption) and (2) electrons near neutral atoms, and (3) bound–free transitions (ionization) (see Section 2 of Supplementary Information). We used generic formulae for the first two contributions and a hydrogen-like atom approximation, which has proved useful even for many-electron systems, for the third (ref. 21, and S.H., S.G. and D.L., manuscript in preparation). The total absorption coefficient (the inverse of the absorption length) at wavelength λ is obtained as the sum of the three terms, $\kappa_\lambda[T] = \kappa_\lambda^{(1)}[T] + \kappa_\lambda^{(2)}[T] + \kappa_\lambda^{(3)}[T]$. The emitted light power per wavelength interval (spectral radiance) follows from $R(t)$, $T(t)$, and $\kappa_\lambda[T(t)]$ (see Section 3 of Supplementary Information):

$$P_\lambda(t) = 4\pi^2 R^2 I_\lambda^{Pl}[T(t)] \times \left(1 + \frac{\exp(-2\kappa_\lambda R(t))}{\kappa_\lambda R(t)} + \frac{\exp(-2\kappa_\lambda R(t)) - 1}{2\kappa_\lambda^2 (R(t))^2}\right) \quad (1)$$

Here, $I_\lambda^{Pl}[T(t)]$ is the Planck intensity emitted from a black body at temperature $T(t)$. The formula simplifies to the spectral radiance of a black body in the limit of $\kappa_\lambda R \to \infty$ and to that of a transparent emitter (the usual case for an SBSL bubble) with $P_\lambda \propto (\kappa_\lambda R) I_\lambda^{Pl}$ for small $\kappa_\lambda R$. P_λ inherits (via κ_λ) the sensitive dependence of $\alpha \propto \exp(-E_{ion}/2k_BT)$ on the temperature. This explains both the shortness of the pulse widths (the intensity is 'turned off' very quickly) and their approximate wavelength independence, as $\exp(-E_{ion}/2k_BT)$ does not vary with λ.

As photon absorption and emission must balance in local thermodynamic equilibrium (Kirchhoff's law), every contribution to the absorption corresponds to a light emission process. Sonoluminescence is therefore generated by thermal bremsstrahlung (the inverse process of (1), (2)) and recombination radiation (inverse of (3)).

Figure 1a shows examples for the spectral radiance following from equation (1) for strongly driven argon and xenon bubbles in water. They are in good agreement with experiment (not shown: compare ref. 3), and the stronger light emission for xenon (mainly

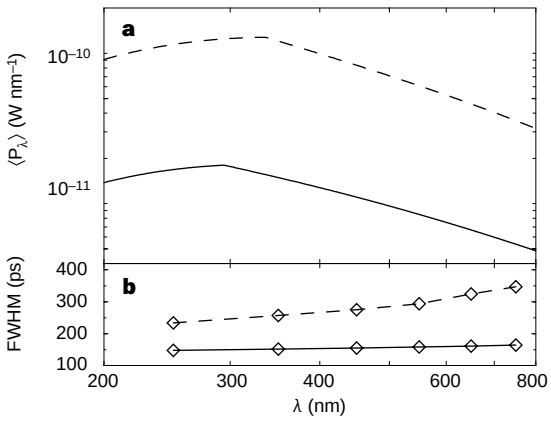

Figure 1 Spectral variation of intensity and pulse width of sonoluminescence pulses from xenon and argon bubbles. **a**, Spectral radiance from an argon (solid line) and a xenon (dashed) bubble, for $P_a = 1.3$ atm, $R_0 = 5.0$ μm. The intensity and shape of the experimentally reported spectra is reproduced very well (compare ref. 3), although the measured spectra decay slightly faster towards the red. **b**, The variation of pulse width with λ, computed for the total power contained in intervals of $\Delta\lambda = 100$ nm. This corresponds to experiments using filters of ~100 nm bandwidth[12].

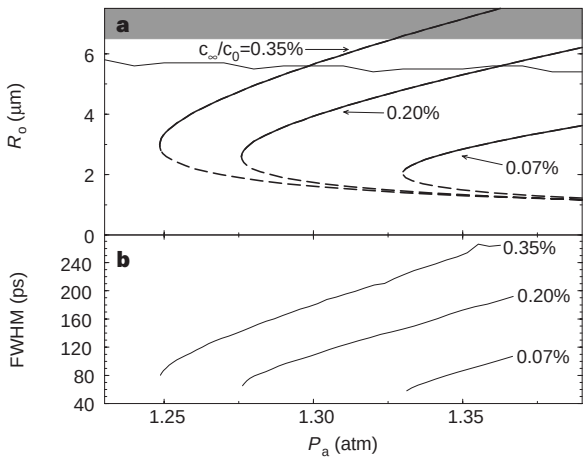

Figure 2 Size and light emission of diffusively stable argon bubbles. **a**, Curves $R_0(P_a)$ of stable (solid thick lines) and unstable (dashed) diffusive equilibria for $f = 20$ kHz at dissolved gas concentrations $c_\infty/c_0 = 0.07\%$, 0.20% and 0.35% (ref. 13), all given relative to the gas solubility c_0. The parametric surface instability restricts R_0 to ~5.5 μm (calculated[6], thin solid line) or ~7 μm (experimental[23], hatched region). **b**, Calculated pulse widths for the stable combinations of P_a and R_0 from **a**. The pulse widths and their dependence on P_a are in good agreement with experiments[13].

due to its lower ionization energy) at equal parameters is reproduced. For both gases, a spectral maximum is predicted. It results from an absorption edge which reflects the detailed energy level structure of the noble gases (S.H, S.G. and D.L., manuscript in preparation). In reality, these maxima should lie at somewhat smaller λ as the level structure becomes modified at the high pressures inside the collapsed bubble. For xenon, the spectral maximum has been observed (at ~300 nm (ref. 3)); for argon, the experiments are not conclusive because of the light absorption of water which modifies the spectrum below $\lambda \approx 250$ nm. Figure 1b confirms that the full-width at half-maximum for the argon bubble shows practically no dependence on λ (as in experiment[12,13,15]), whereas the present model predicts a quite pronounced variation of the largest and brightest xenon bubbles (though much smaller than in the black-body case). This variation should be detectable and awaits experimental verification.

A significant advantage of the present approach is the possibility to scan the whole parameter space of SBSL, because the calculations are very simple, and thus to reproduce experimentally observed parameter dependences of SBSL light emission. In experiment, the driving frequency f, the forcing pressure P_a, the water temperature T_w, and the noble gas concentration c_∞ in the liquid far away from the bubble are the crucial adjustable parameters. To calculate $R(t)$, we need the bubble's ambient radius R_0 (radius of a stationary, undriven bubble) for given f, P_a, T_w, and c_∞. It has been shown[6,22] that $R_0(f, P_a, T_w, c_\infty)$ is given by the condition of diffusive stability (dynamical equilibrium of gas exchange between the bubble interior and the surrounding liquid).

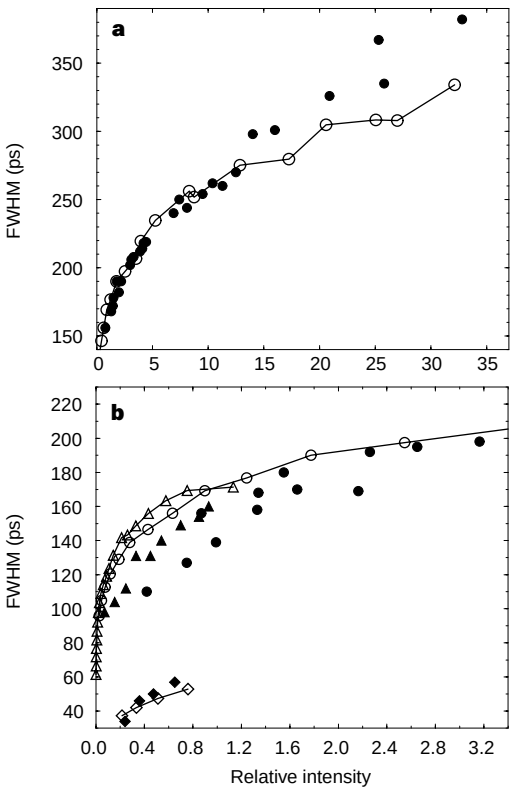

Figure 3 Calculated and measured sonoluminescence pulse widths as a function of light intensity. Open symbols denote theoretical results and filled symbols (from ref. 15) experimental data for $f = 34$ kHz. The larger experimental values for width and intensity are obtained for smaller water temperature, where the bubbles can be driven harder. **a**, Data for diffusively stable xenon bubbles at $c_\infty/c_0 = 0.4\%$. **b**, Diffusively stable Ar (triangles) and Xe (circles) bubbles, again for $c_\infty/c_0 = 0.4\%$. In addition, the values for $c_\infty/c_0 = 0.03\%$ argon are shown (diamonds), corresponding to the experiment on air at a partial pressure of 20 mm Hg (ref. 15).

Figure 2a shows the curves of diffusive equilibria in P_a–R_0 space (the branches with positive slope being stable) for several gas concentrations c_∞ used in experiment[12,13]. As the experimenter changes P_a, the corresponding curve determines the response of the ambient size R_0 of the SBSL bubble, and calculating the light emission for these specific pairs (P_a, R_0) should therefore reproduce the measured photon numbers, pulse widths, and so on. The upper limits for P_a and R_0 are imposed by the onset of shape instabilities (compare Fig. 2a and refs 6, 23 and 24. Figure 2b shows the results for the widths (full-width at half-maximum) of the emitted SBSL pulses, as a function of P_a. The range of pulse widths is in excellent agreement with experiment. The shift in the P_a axis (~0.10–0.15 atm) with respect to the data in ref. 13 could be due to the simplified modelling, but also to experimental inaccuracies of at least 0.1 atm in measuring P_a (B. Gompf, personal communication).

A more stringent test of the theory presented here can be made by comparing its predictions to the extensive experimental data of Hiller *et al.*[15] on spectral pulse widths and intensities, both of which are accurately measurable quantities. In ref. 15, the intensity values are given relative to the maximum intensity of an air bubble dissolved in water at 150 mm Hg partial pressure. This normalizing intensity was determined with the present model (the relevant partial pressure being only that of argon (that is 1.5 mm Hg), because of molecular dissociation), and used as the intensity unit for all theoretical results in Fig. 3. In Fig. 3a we compare for xenon bubbles the experimentally found dependence of FWHM on intensity (filled symbols) to our calculations (open symbols). The agreement is, despite the approximations involved in the model, excellent. Not only is the qualitative shape of the curve reproduced, but also a quantitative comparison shows that the pulse widths differ from the experimental values by no more than ~5% for moderate intensities, and by no more than ~15% for high intensities. Other features from experiment are reproduced in Fig. 3b for argon and xenon bubbles in the range of smaller intensities. We note first that both argon and xenon bubbles follow almost exactly the same line in this diagram, if the same noble-gas concentration is applied (here, $c_\infty/c_0 = 0.4\%$), although the values of P_a and R_0 are quite different at a given intensity. Second, the theory also reproduces the tiny pulse widths and intensities if air at 20 mm Hg partial pressure is used instead of Ar or Xe (Fig. 3b, bottom left), corresponding to a relative argon concentration of 0.03%. □

Received 25 June 1998; accepted 21 January 1999.

1. Gaitan, D. F. *An Experimental Investigation of Acoustic Cavitation in Gaseous Liquids.* Thesis, Univ. Mississippi (1990).
2. Crum, L. A. Sonoluminescence. *Phys. Today* **47,** 22–29 (1994).
3. Barber, B. P., Hiller, R. A., Löfstedt, R., Putterman, S. J. & Weninger, K. R. Defining the unknowns of sonoluminescence. *Phys. Rep.* **281,** 65–143 (1997).
4. Brennen, C. E. *Cavitation and Bubble Dynamics* (Oxford Univ. Press, 1995).
5. Brenner, M. P., Lohse, D. & Dupont, T. Bubble shape oscillations and the onset of sonoluminescence. *Phys. Rev. Lett.* **75,** 954–957 (1995).
6. Hilgenfeldt, S., Lohse, D. & Brenner, M. P. Phase diagrams for sonoluminescing bubbles. *Phys. Fluids* **8,** 2808–2825 (1996).
7. Lohse, D., Brenner, M. P., Dupont, T., Hilgenfeldt, S. & Johnston, B. Sonoluminescing air bubbles rectify argon. *Phys. Rev. Lett.* **78,** 1359–1362 (1997).
8. Lohse, D. & Hilgenfeldt, S. Inert gas accumulation in sonoluminescing bubbles. *J. Chem. Phys.* **107,** 6986–6997 (1997).
9. Prosperetti, A. Thermal effects and damping mechanisms in the forced radial oscillations of gas bubbles in liquids. *J. Acoust. Soc. Am* **61,** 17–27 (1977).
10. Prosperetti, A. The thermal behaviour of oscillating gas bubbles. *J. Fluid Mech.* **222,** 587–616 (1991).
11. Moss, W., Clarke, D. & Young, D. Calculated pulse widths and spectra of a single sonoluminescing bubble. *Science* **276,** 1398–1401 (1997).
12. Gompf, B., Günther, R., Nick, G., Pecha, R. & Eisenmenger, W. Resolving sonoluminescence pulse width with time-correlated single photon counting. *Phys. Rev. Lett.* **79,** 1405–1408 (1997).
13. Pecha, R., Gompf, B., Nick, G., Wang, Z. Q. & Eisenmenger, W. Resolving the sonoluminescence pulse shape with a streak camera. *Phys. Rev. Lett.* **81,** 717–720 (1998).
14. Moran, M. J. & Sweider, D. Measurements of sonoluminescence temporal pulse shape. *Phys. Rev. Lett.* **80,** 4987–4990 (1998).
15. Hiller, R. A., Putterman, S. J. & Weninger, K. R. Time-resolved spectra of sonoluminescence. *Phys. Rev. Lett.* **80,** 1090–1093 (1998).
16. Vuong, V. Q. & Szeri, A. J. Sonoluminescence and diffusive transport. *Phys. Fluids* **8,** 2354–2364 (1996).
17. Yuan, L., Cheng, H. Y., Chu, M. C. & Leung, P. T. Physical parameters affecting sonoluminescence: A self-consistent hydrodynamic study. *Phys. Rev. E* **77,** 4265–4280 (1998).
18. Flint, E. B. & Suslick, K. S. The temperature of cavitation. *Nature* **253,** 1397–1399 (1991).
19. Matula, T. J. & Crum, L. A. Evidence for gas exchange in single-bubble sonoluminescence. *Phys. Rev. Lett.* **80,** 865–868 (1998).

20. Ketterling, J. A. & Apfel, R. E. Experimental validation of the dissociation hypothesis for single bubble sonoluminescence. *Phys. Rev. Lett.* **81,** 4991–4994 (1998).
21. Zel'dovich, Y. B. & Raizer, Y. P. *Physics of Shock Waves and High-Temperature Hydrodynamic Phenomena* Vols I & II (Academic, New York, 1966).
22. Fyrillas, M. M. & Szeri, A. J. Dissolution or growth of soluble spherical oscillating bubbles. *J. Fluid Mech.* **277,** 381–407 (1994).
23. Holt, G. & Gaitan, F. Observation of stability boundaries in the parameter space of single bubble sonoluminescence. *Phys. Rev. Lett.* **77,** 3791–3794 (1996).
24. Prosperetti, A. & Hao, Y. Modeling of spherical gas bubble oscillations and sonoluminescence. *Phil. Trans. R. Soc. Lond.* **357,** 203–224 (1999).

Supplementary information is available on *Nature*'s World-Wide Web site (http://www.nature.com) or as paper copy from the London editorial office of *Nature*.

Acknowledgements. We thank S. Koehler, W. Moss and H. Stone for discussions. Support by the DFG and partial support by the NSF is acknowledged.

Correspondence and requests for materials should be addressed to D.L. (e-mail: lohse@tn.utwente.nl).

Immobility of protons in ice from 30 to 190 K

J. P. Cowin*, A. A. Tsekouras†, M. J. Iedema*, K. Wu* & G. B. Ellison‡

* *Pacific Northwest National Laboratory, Box 999, MS K8-88, Richland, Washington 99352, USA*
† *Laboratory of Physical Chemistry, University of Athens, Athens GR-15771, Greece*
‡ *Department of Chemistry & Biochemistry, University of Colorado, Boulder, Colorado 80309, USA*

The anomalously fast motion of hydronium ions (H_3O^+) in water is often attributed to the Grotthuss mechanism[1,2], whereby protons tunnel from one water molecule to the next. This tunnelling is relevant to proton motion through water in restricted geometries, such as in 'proton wires' in proteins[3] and in stratospheric ice particles[4]. Transport of hydronium ions in ice is thought to be closely related to its transport in water[1,2]. But whereas claims have been made that such tunnelling can persist even at 0 K in ice[5–7], counter-claims suggest that the activation energy for hydronium motion in ice is non-zero[8–10]. Here we use 'soft-landing'[11–13] of hydronium ions on the surface of ice to show that the ions do not seem to move at all at temperatures below 190 K. This implies not only that hydronium motion is an activated process, but also that it does not occur at anything like the rate expected from the Grotthuss mechanism. We also observe the motion of an important kind of defect in ice's hydrogen-bonded structure (the D defect). Extrapolation of our measurements to 0 K indicates that the defect is still mobile at this temperature, in an electric field of 1.6×10^8 V m^{-1}.

Water's hydrogen-bonded network must be disrupted to solvate or transport ions. Figure 1 shows the hydrogen bonding in a thin film of water. Normally, each water molecule hydrogen-bonds with four neighbours. Three hydronium ions were initially placed on top of the film. At right, a proton has hopped four monolayers down, via the Grotthuss mechanism. Figure 1 shows D and L defects, which are misdirected hydrogen bonds, that put either two or zero protons between two adjacent oxygens instead of the usual one proton. These D/L defects facilitate the re-orientation of water molecules, creating water's high solvation power and dielectric constant ϵ.

The ions in Fig. 1 will move in their collectively self-generated electric field $|E|$. When all ions are at the top of a film (of thickness b) on an earthed substrate, this gives a 'film voltage' ΔV of

$$\Delta V = |E|b = \frac{Qb}{A\epsilon\epsilon_0} \quad (1)$$

where charge Q is deposited over area A, and ϵ_0 is the vacuum permittivity. The ion motion could be measured by the time-dependent current induced between an electrode placed on top of the film and the substrate, as in the classical 'proof' of proton tunnelling, the 95–180 K study by Eckener *et al.*[5] They used 0.5-J laser pulses to "stimulate" the release of hydronium ions from hydrogen-gas-pretreated Pd powder. The powder was pressed onto one face of ice crystal wafers 90–300 μm thick; the opposing face was a biased electrode. However, these difficult experiments (never duplicated) are prone to artefacts[10,14]. "Proton injection" experiments at much higher temperatures also claim a zero activation

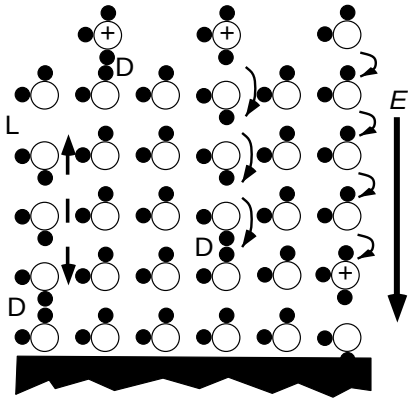

Figure 1 Ice structure and transport. A diagram of ice's hydrogen-bonding network is shown. On top were placed three hydronium ions (+). L and D hydrogen-bond defects are also present. At the top, 'soft-landed' hydronium ions form D defects. At right the hydronium ion's proton, in an electric field E, has hopped to an adjacent water four times, changing the hydronium's position. In the centre, a D defect moves away from the hydronium. At left, an L/D-defect pair formed and diffused apart.

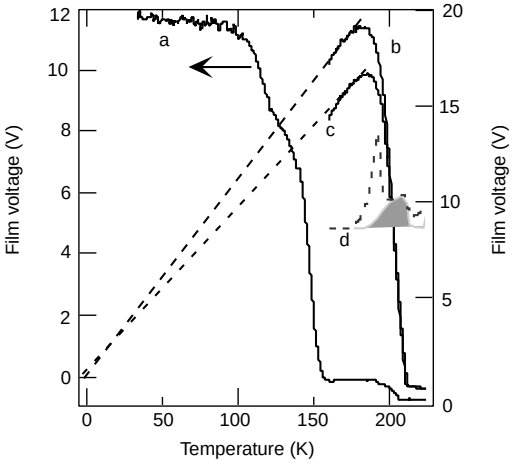

Figure 2 Lack of diffusion of hydronium ions in water ice. Data are shown for crystalline water films dosed with hydronium ions. Trace a, 2,880 monolayers (ML) grown at 150 K, ion-dosed (20 nC) at 33 K. Voltage (left axis) is shown as temperature T is increased at 0.167 K s^{-1}. Trace b, 5,980 ML grown at 165 K, then ion-dosed (700–3,800 nC) at 165 K. Trace c, 820 ML dosed at 165 K, ion dosed (600–1,900 nC) at 165 K, then water dosed (480 ML) at 165 K. (Traces b, c use right axis.) Water desorption occurs near 200 K for these thick films (trace d, shown for 5,980 ML film). Maximum ion dose is 2.6% of a monolayer. The water desorption curve is double-peaked, as the Kelvin probe slows desorption from the region behind it. The shaded portion is the desorption peak to compare to the work-function changes. ϵ was measured to be about 2.3 ± 33% for the start of trace a, and 160 (±50%) for the start of curves b and c. Voltage remaining high from 33 to 150 K (trace a) and from 160 to 190 K shows that hydronium ions do not move in these temperature ranges. Dashed curve is the expected behaviour from equation (1), for ϵ proportional as $1/T$, if hydronium ions do not move.